Energy & Environmental Science

Accepted Manuscript

This article can be cited before page numbers have been issued, to do this please use: J. Yang, Y. Kang, F. Meng, W. meng, G. Chen, M. Zhang, Z. Lv, Z. Wen, C. Li, J. Zhao and Y. Yang, *Energy Environ. Sci.*, 2024, DOI: 10.1039/D4EE04119D.

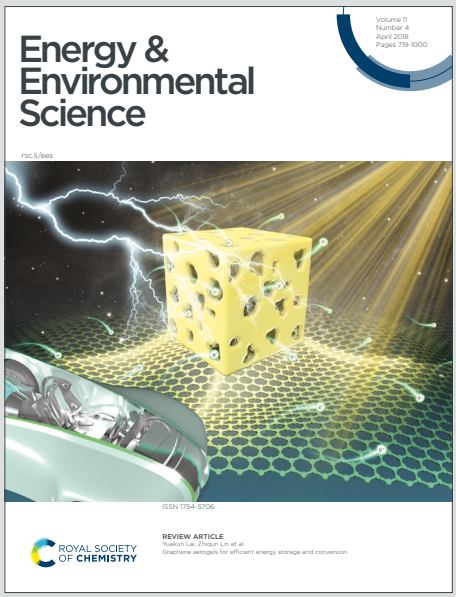

ROYAL SOCIETY OF CHEMISTRY

rsc.li/ees

View Article Online
DOI: 10.1039/D4EE04119D

Broader context

Aqueous Zn-I_2 batteries, known for their high safety due to the use of aqueous electrolytes and environmentally friendly cathode and anode materials, face limitations caused by the polyiodide shuttle effect and the slow kinetics of iodine redox reactions. While various single-atom catalysts (SACs) have been suggested to enhance their electrochemical performance, the identification of optimal SACs remains unclear due to the diversity of d-block transition metals. Previous studies have primarily focused on binding energies and reaction free energies during discharge, with limited exploration of how the d-electron structure of SACs affects catalytic activity. Understanding this relationship is critical, as the d-electron structure influences chemical bonding and reactivity. In this study, comprehensive theoretical calculation results demonstrate that the primary interaction between iodine species and d-block SACs is mediated by d-p orbital hybridization. Nb-NC was identified as the optimal candidate due to its numerous unfilled antibonding orbitals, which promote effective d-p hybridization. As a result, Nb-NC, with a low d-band center of 0.271 eV, demonstrates the strongest polyiodide binding energy and the lowest reaction barrier for the rate-limiting step ($I_3^- \rightarrow I^-$). The assembled Zn||Nb-NC/I_2 battery delivers an outstanding stability.

View Article Online
DOI: 10.1039/D4EE04119D

ARTICLE

Theoretical calculations-driven rational screening of d-block single-atom electrocatalysts based on d-p orbital hybridization for durable aqueous zinc-iodine batteries

Received 00th January 20xx,
Accepted 00th January 20xx

DOI: 10.1039/x0xx00000x

Jin Yang,†[a] Yuanhong Kang,†[a] Fanxiang Meng,[a] Weiwei Meng,[b] Guanhong Chen,[a] Minghao Zhang,[a] Zeheng Lv,[a] Zhipeng Wen,[c] Cheng Chao Li,*[c] Jinbao Zhao,*[a] and Yang Yang*[a]

Aqueous Zn−iodine ($Zn-I_2$) batteries, featuring intrinsically high-safety aqueous electrolytes and eco-friendly cathode/anode materials, however are restricted by the shuttling of polyiodide and sluggish redox kinetics of iodine redox. Although various single atom catalysts (SACs) have been proposed to improve the electrochemical performance, the underlying mechanisms of different SACs involved in iodine redox are not completely elucidated. Herein, the interaction between d-block SACs and polyiodide is demonstrated to follow d-p orbital hybridization theory, thus a series of SACs with different d-block transitional metal sites are pre-screened using DFT calculations to assess the hybridization effectiveness. Among these, Nb-NC is selected due to its numerous unfilled antibonding orbitals, which facilitate effective d-p hybridization between Nb-d and I-p orbitals. Accordingly, Nb-NC with a low d-band center of 0.271 eV exhibits the highest binding energy for polyiodide and the lowest reaction barrier for the rate-determining step ($I_3^- \rightarrow I^-$). These theoretical predictions are well corroborated by various in/ex situ characterizations, which confirm the suppressed shuttle effect and enhanced redox conversion of iodine species by using a free-standing Nb-NC/I_2 cathode. Consequently, the Zn||Nb-NC/I_2 battery can maintain an exceptional capacity of 140 mA h g^{-1} over 50,000 cycles at 10 A g^{-1}, with only 0.00008% capacity decay per cycle.

Introduction

The escalating global climate concerns have spurred intensive research into renewable and clean energy sources, such as wind and solar power.[1] However, due to their inherent intermittent, effective energy storage devices are imperative to harness maximum energy. Aqueous zinc-ion batteries (AZIBs) are one of the most competitive options to conventional lithium-ion batteries due to their affordability, environmental compatibility, and non-flammability.[2–5] Among various AZIB systems, zinc–iodine ($Zn–I_2$) batteries stand out due to the abundance of iodine (55 mg per liter seawater), the relatively high theoretical capacity (211 mAh g^{-1} based on I^-/I^0 redox couple), and a satisfactory working potential (1.38 V vs. Zn^{2+}/Zn).[6–12] Despite their potential advantages, the sluggish redox kinetics between iodine species and the shuttle effect of polyiodide significantly impede the actual electrochemical performance and cycling lifespan of $Zn–I_2$ batteries.[13–18] To address these problems, the most widely used strategy is to confine iodine with carbon-based hosts, which can accommodate I_2 in their porous structure and improve electronic conductivity.[19–21] Nevertheless, the weak physisorption of nonpolar carbon frameworks can not completely prevent the formation and transfer of polyiodide, especially as the adsorption sites become saturated at high polyiodide concentrations. Therefore, enhancing the rate of iodine reduction reactions by electrocatalysts is a significant approach for realizing high-performance $Zn–I_2$ batteries.

Single-atom catalysts (SACs), are a unique class of electrocatalysts characterized by isolated individual metal atoms uniformly dispersed on a carrier without any interaction between the metal atoms.[22] Due to the maximum atom utilization, SACs are extremely easy to chemically interact with reactive species, thus exhibiting ultra-high intrinsic activity.[23,24] The d-p hybridization theory has been utilized in Li-S batteries to explain the efficient catalytic mechanism of SACs. When SACs adsorb sulfur intermediates, the hybridization state between the d orbitals of SACs and the p orbitals of sulfur will change the electronic structure of adsorbates, which will in turn lower the reaction energy barrier. Considering that both iodine and sulfur have unfilled p-orbitals (The outer electron arrangement of iodine is $5s^25p^5$, while that of sulfur is $3s^23p^4$), iodine can also hybridize with the d orbitals of transition metals to form d-p hybridized orbitals. Recent investigations have explored the applications of SACs including Ni, Fe, Co, and Cu to facilitate the iodine reduction reactions within the $Zn-I_2$ battery framework,

[a] State Key Laboratory of Physical Chemistry of Solid Surfaces, State-Province Joint Engineering Laboratory of Power Source Technology for New Energy Vehicle, College of Chemistry and Chemical Engineering, Xiamen University, Xiamen, 361005, P. R. China. E-mail: jbzhao@xmu.edu.cn, yangyang419@xmu.edu.cn
[b] Key Laboratory of Functional Materials and Devices for Special Environments of CAS, Xinjiang Key Laboratory of Electronic Information Materials and Devices; Xinjiang Technical Institute of Physics & Chemistry of CAS, Urumqi, 830011, P. R. China
[c] School of Chemical Engineering and Light Industry, Guangdong University of Technology, Guangzhou, 510006, P. R. China. E-mail: licc@gdut.edu.cn
† These authors contribute equally to the work.
Supplementary Information available: [XPS, BET, electrochemical tests and calculation results]. See DOI: 10.1039/x0xx00000x

View Article Online DOI: 10.1039/D4EE04410D

achieving good rate capability and improved cycling stability.[25–29] It can be inferred that the active sites of these reported SACs are mainly focused on d-block traditional metals, which possess partially filled d bands, exhibiting great potential for chemical interactions and catalytic conversion of polyiodides. Considering the diversity of d-block traditional metal species, identifying the "right" SACs for achieving high-performance Zn-I_2 batteries is still ambiguous. On the other hand, previous research has often evaluated the catalytic effects of SACs by examining binding energies and conversion reaction free energies during the discharging process, while the intrinsic interaction mechanisms between SACs and iodine species, particularly the influence of the d-electron structure of SACs on catalytic activity have been less explored. Understanding this relationship is crucial, as the d-electron structure plays a crucial role in determining the chemical bonding and reactivity of the active sites. Therefore, establishing a correlation between the polyiodide conversion reaction and d-electron structure of SACs may unlock potential opportunities for developing high-performance electrocatalysts that are more efficient in inhibiting the shuttling effect in Zn-I_2 batteries.

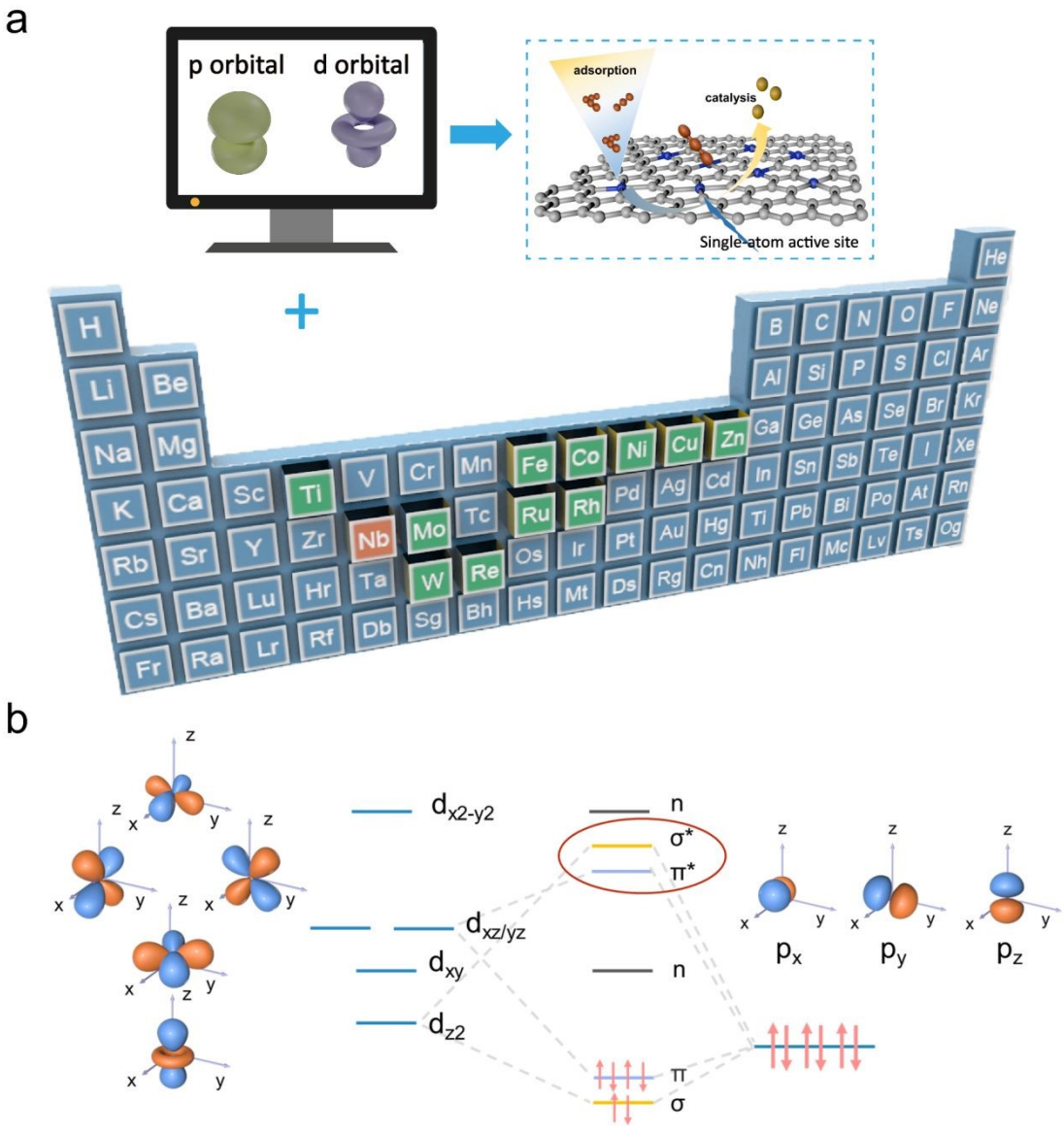

Fig. 1 (a) Schematic illustration of iodine species adsorption and catalysis on M-Nc (M= Co, Cu, Fe, Nb, Ni, Zn, Mo, Re, Rh, W, Ru, and Ti). (b) Scenario of d-p orbital hybridization.

View Article Online
DOI: 10.1039/D4EE04110D

In this work, DFT (density functional theory) calculations are utilized as a preliminary strategy to explore how different d-block SACs in the form of M-N_4 (M= Co, Cu, Fe, Nb, Ni, Zn, Mo, Re, Rh, W, Ru, Ti) configurations affect the polyiodide conversion reaction (Figure 1a). Comprehensive theoretical calculation results reveal that the primary interaction between iodine species and transitional metal active site of SACs is mediated by d-p orbital hybridization (Figure 1b). The d-electron structure of SACs will affect the interaction with polyiodide based on the different d-p orbital hybridization effectiveness, which is directly related to binding strengths and conversion reaction energy barriers. Among different d-block SACs studied, Nb possesses fewer d-orbital electrons and a rearrangement of the d-orbital energy levels is verified in Nb-NC. Accordingly, the increase in $d_{xz}/_{yz}$ orbital energy levels and decrease in d_{xy} and d_{x2-y2} orbital energy levels leads to prioritized bonding orbitals electron occupation. Therefore, Nb–NC with abundant unfilled antibonding states and a d-band center of 0.271 eV near the Fermi level, enables more effective d–p orbital hybridization, thus providing a strong iodine affinity and rapid iodine redox kinetics. Furthermore, Nb-NC exhibits the lowest reaction barrier for the rate-determining step ($I_3^- \rightarrow I^-$), which improves the redox reversibility of iodine species. Motivated by this theoretical proposal, Nb-NC is synthesized and adopted as an efficient electrocatalyst for Zn-I_2 batteries. Various in/ex situ experimental characterizations demonstrate that the shuttle effect of polyiodide is effectively suppressed and the electrocatalytic redox conversion of iodine is enhanced. Due to the high catalytic-active sites in the conductive network, iodine species can be well confined in Nb-NC electrocatalysts, allowing for the fabrication of self-standing I_2 electrodes, which can further increase the battery energy density by eliminating the utilization of traditional current collectors. As a result, the Nb-NC/I_2 cathode could endow an inspiring durability of 1700 h (an ultrahigh retention ratio of 96% at 10 A g^{-1} over 50,000 cycles).

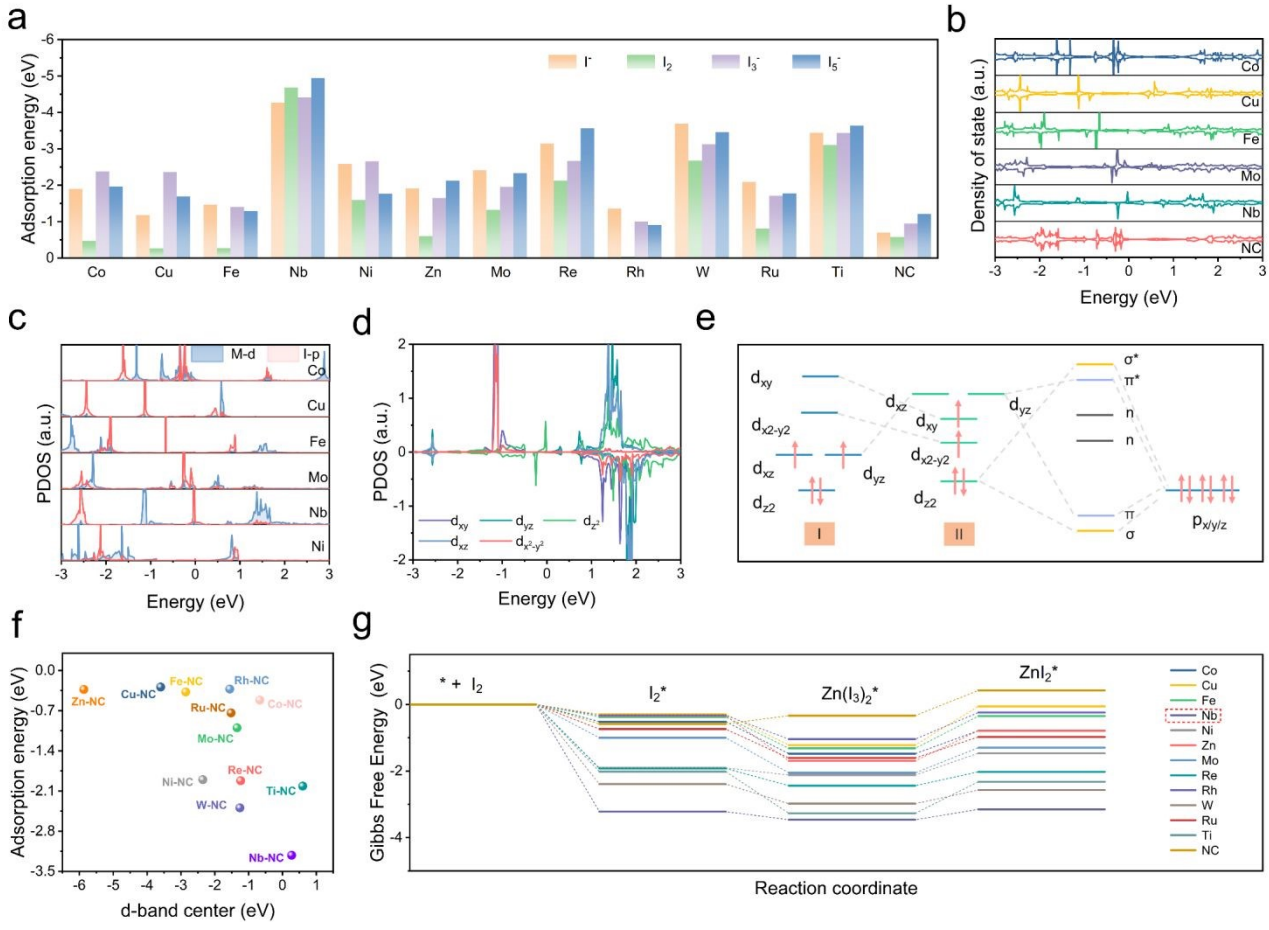

Fig. 2 (a) Comparison of adsorption energy between M-NC (M = Co, Cu, Fe, Nb, Ni, Zn, Mo, Re, Rh, W, Ru, and Ti) and NC for I^-, I_2, I_3^-, and I_5^-. (b) DOS for the different M-NC (M = Co, Cu, Fe, Mo, and Nb) and NC. (c) PDOS of the p orbital of I and d orbital of M-NC (M = Co, Cu, Fe, Mo, Nb, and Ni). (d) PDOS of Nb-d orbitals. (e) Scenario of d-p orbital hybridization. (f) The relationship between the d-band center of different SACs and the adsorption energies for I_2*. (g) Gibbs free energy for reduction of iodine on M-NC (M = Co, Cu, Fe, Nb, Ni, Zn, Mo, Re, Rh, W, Ru, and Ti) and NC.

Results and discussion

A series of DFT computations were performed on twelve typical monatomic electrocatalysts with M-N_4 configurations (M= Co, Cu, Fe, Nb, Ni, Zn, Mo, Re, Rh, W, Ru, Ti). These computations aim to evaluate the interaction between the electrocatalysts and various iodine species, which are crucial for enhancing the performance of Zn-I_2 batteries. Firstly, as a good indicator, the adsorption energies of M-NCs on various iodine species were calculated and compared to those of metal-free nitrogen-doped carbon (NC) (Figure 2a and S1). The calculation results show that adsorption energies of M-NCs on iodine species are all higher than those of pure NC and Nb-NC possesses the largest values of -4.27 eV, -3.22 eV, -3.63 eV, and -3.92 eV for I^-, I_2, I_3^-, and I_5^- respectively, suggesting the potential of Nb-NC for adsorption catalysis on iodine species. Besides, total density of states (DOS) results reveal that the energy bands of Co, Nb, Re, Rh, Ru, Ti, W, and Zn extend across the Fermi energy level (0 eV), indicating that these corresponding M-NCs possess excellent electrical conductivity (Figure 2b and S2). On the contrary, NC without metal active centers has a wide band gap, which is not conducive to efficient electron transfer. For effective electrocatalysts, the d orbitals of transition metal elements play a key role in hybridizing with adsorbed intermediates, which influences the potential hybridization between the M-d orbitals and the I-p orbitals. To reveal the intrinsic interaction mechanism between SACs and iodine species and to understand how d-electron structure of SACs affects their catalytic activity, the electronic structures of the SAC-ZnI_2 systems were analyzed. As displayed in Figure 2c, and S3, a higher degree of overlap between Nb-d orbitals and I-p orbitals is observed compared to other SACs, suggesting the efficient d-p hybridization. Coordination field theory was applied to further explore the electronic structure of Nb-NC. It has been demonstrated that d_{z2} and $d_{xy}/_{yz}$ states of the SAC with the M-N_4 configuration is more oriented towards D_{4h} crystal field.[23] The five d orbitals are d_{xy}, d_{x2-y2}, $d_{xz}/_{yz}$ (two-fold degenerate), and d_{z2} in descending order of energy level (Figure 2e, I). Upon adsorption of iodine species, the energy levels of $d_{xz}/_{yz}$ and d_{z2} increase, while those of d_{xy} and d_{x2-y2} reduced (Figure 2d, Figure 2e, II). This energy level shift is contributed to the structural change of Nb-NC for iodine (Figure S1), where the Nb atom slightly protrudes from the substrate, facilitating effective d-p orbital hybridization.

More specifically, it is clear that the d_{xz} and d_{yz} demonstrate the highest energy and are not electronically populated, while d_{z2}, d_{xy}, and d_{x2-y2} are electronically populated. The overlap of the p_z orbital of the iodine atom with the d_{xz} of Nb suggests the formation of σ and σ* states (Figure S4). Similarly, twofold π and π* states derived from the hybridization of the $d_{xz}/_{yz}$ orbitals with the $p_{x/y}$ orbitals, while d_{xy} and d_{x2-y2} do not bond with the p orbitals (non-bonding states). Subsequently, after the rearrangement of energy levels in the d orbitals of Nb-NC, electrons preferentially occupy the bonding orbitals, leading to the effective d-p hybridization between Nb-d orbitals and I-p orbitals, thus enhancing the adsorption and redox kinetics of iodine species. It is noteworthy that elements with many electrons in the d orbitals will have their antibonding orbitals gradually filled, resulting in weak bonding strength. In addition to the efficient d-p orbital hybridization, the d-band center serves as a vital indicator for evaluating the electrical conductivity and catalytic properties of SACs. As depicted in Figure 2f and Table S1, the d-band center of Nb-NC is only 0.271 eV close to the Fermi energy level, corresponding to the high adsorption energy for I_2 up to -3.22 eV. To further assess the catalytic effect of SACs on the I_2 reduction reaction, the Gibbs free energies of I_2 reduction pathways in different M-NCs, and NC were given in Figure 2g. The full reduction reaction pathway can be summarized as follows: $I_2 \rightarrow I_2^* \rightarrow Zn(I_3)_2^* \rightarrow ZnI_2^*$, with two important intermediates of I_2^* and I_3^* being considered in this analysis. In the overall reduction reaction ($I_2 \rightarrow ZnI_2^*$), the more negative Gibbs free energy of Nb-NC suggests that the reaction is most likely to occur in the presence of Nb-NC. Moreover, for many electrocatalysts, the reaction path ($I_3^- \rightarrow I^-$) is identified as the rate-determining step in the reduction process. In the presence of Nb-NC, the reaction energy barrier for this decisive step is found to be the lowest among these M-NCs studied, further demonstrating that the Nb-N_4 configuration, with Nb serving as the metal active center is most favorable for catalyzing and accelerating redox kinetics of iodine. This combination of a low d-band center, strong adsorption energy of iodine species, and a low reaction energy barrier highlights Nb-NC as a highly effective electrocatalyst for Zn-I_2 batteries, which is expected to significantly enhance their electrochemical performance and cycling stability.

To investigate the practical feasibility of Nb-NC as an efficient electrocatalyst for Zn-I_2 batteries, Nb-NC and Fe-NC were successfully synthesized according to previous work.[23] The microstructure of Nb-NC was examined by using transmission electron microscopy (TEM), revealing a dodecahedral morphology with an average size of approximately 160 nm (Figure 3a). Moreover, the high-angle annular dark-field scanning transmission electron microscopy (HAADF-STEM) image shows the atomic dispersion of the Nb metal on the carbon skeleton (Figure 3b). The successful incorporation of Nb was also validated by the energy dispersive spectroscopy (EDS) elemental mapping result (Figure 3c). Furthermore, the elemental composition and chemical environments of NC and Nb-NC were further characterized by X-ray photoelectron spectroscopy (XPS). A weak peak located at 207.1 eV in the Nb-NC spectrum corresponds to the Nb element (Figure S5a). Additionally, the C-N peaks at 285.6 eV confirm the introduction of electron-accepting N atoms, which allows the surrounding C atoms to form a more positive surface, thus enhancing iodine chemisorption through polarization interactions, rather than relying solely on the physical confinement offered by the porous structure (Figure 3d and S5b). The coordination form of Nb-N is also corroborated by the emergence of a peak at 399.6 eV in the N 1s spectrum (Figure 3e and S5c). Besides, the peaks in the Nb 3d spectrum of 204.3 and 206.9 eV are indicative of the presence of Nb^{4+} (Figure 3f), which tentatively demonstrates that the synthesized Nb-NC adopts the Nb-N_4 configuration.

View Article Online
DOI: 10.1039/D4EE04119D

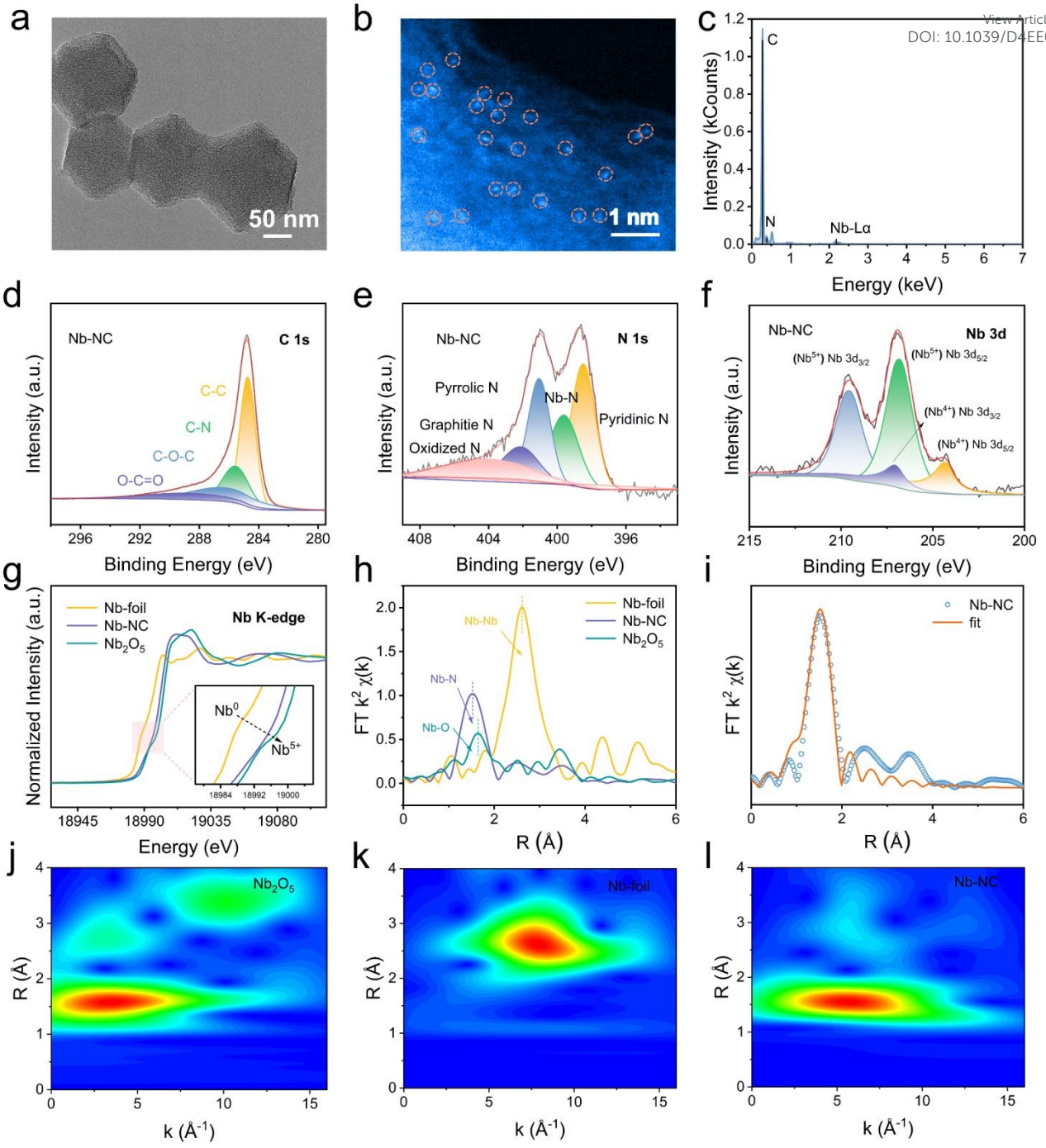

Fig. 3. (a) TEM image, (b) HAADF-STEM image, (c) STEM-EDS elemental mapping of Nb-NC. (d) XPS high-resolution spectra of C 1s, (e) N 1s, and (f) Nb 3d for Nb-NC. (g) Nb K-edge XANES spectra, (h) FT-EXAFS spectra for Nb-foil, Nb-NC, and Nb_2O_5. (i) EXAFS spectra and the curve-fit in R-space for Nb-NC. WT of EXAFS plots of (j) Nb_2O_5, (k) Nb-foil, and (l) Nb-NC.

To further clarify the coordination number, valence, bond length, and electronic structure of the Nb single atoms, X-ray absorption near edge structure (XANES) measurements were carried out. The adsorption edge for Nb-NC in Nb-K edge XANES spectra is located between Nb foil and N_2O_5, indicating that the average valence state of Nb in Nb-NC is between 0 and +5 (Figure 3g). The peak attributed to Nb-N (1.52 Å) is detected for Nb-NC in the extended X-ray absorption fine structure (EXAFS) spectra via Fourier transform (FT) in R-space, while peaks corresponding to Nb-O (1.65 Å) and Nb-Nb (2.62 Å) are notably absent (Figure 3h). Furthermore, the EXAFS spectra for Nb-NC, Nb foil, and Nb_2O_5 were fitted to the R-space to analyze their coordination environments (Figure 3i, S6, and Table S2). The coordination number of Nb-N in Nb-NC is confirmed to be 4.0 ± 0.5 with a bond length of 2.08 Å, validating the Nb-N_4 conformation as the predominant structure. Given the similarity between the Nb-N and Nb-O peaks in the EXAFS spectra, a high-resolution wavelet-transform (WT) analysis of

View Article Online
DOI: 10.1039/D4EE04119D

EXAFS was performed. As can be seen in Figure 3l, the WT plot of Nb-NC shows Nb-N scattering maximum at 5.59 Å^{-1}, further validating the form of Nb-N and confirming the absence of Nb-Nb and Nb-O (Figure 3j and 3k). These analytical results verify the successful synthesis of Nb-NC in the form of Nb-N_4 conformation. In addition, the pore structure of Nb-NC and NC were analyzed using low temperature nitrogen adsorption and desorption tests (Figure S7). Both NC and Nb-NC exhibit isotherms with typical type IV characteristics, indicating a composition of microporous and mesoporous structures. Specifically, Nb-NC exhibits a large specific surface area (755.96 m^2 g^{-1}) and a relatively wide size distribution centered at 1.74 nm. The larger I_D/I_G ratio of Nb-NC (1.073) compared to NC (1.058) in Raman tests further indicates a higher density of defect/edge sites (Figure S8). Such a porous and defective structure enlarges contact areas between iodine and Nb for efficient electrocatalysis. The corresponding material characterizations of Fe-NC are also shown in Figure S9 and S10.

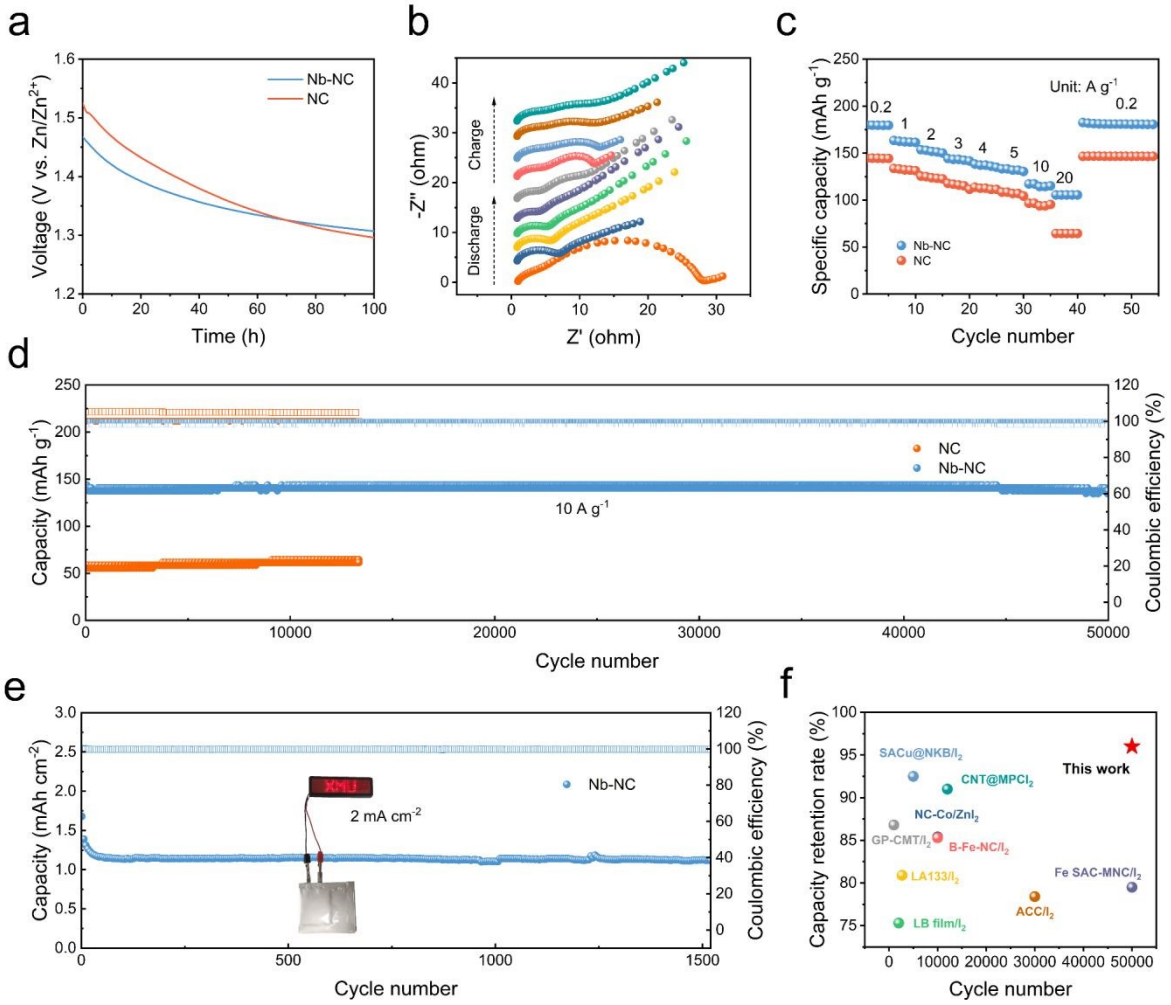

Fig. 4. (a) Self-discharge curves of Zn-I_2 batteries with NC/I_2 and Nb-NC/I_2 electrodes. (b) In situ EIS characterization of Zn-I_2 batteries with Nb-NC/I_2 electrode. (c) Rate performance of Zn-I_2 batteries with NC/I_2 and Nb-NC/I_2 electrodes. (d) Long cycle performance test of Zn-I_2 batteries with NC/I_2 and Nb-NC/I_2 electrodes at a current density of 10 A g^{-1}. (e) Long cycle performance test of pouch batteries with Nb-NC/I_2 electrode at 2 mA cm^{-2}. (f) Comparison of Nb-NC/I_2 electrode with other representative I_2 electrodes.

To verify the adsorption and catalytic effect of Nb-NC in Zn-I_2 batteries, Nb-NC was mixed with I_2 by a dry-cast process to fabricate a self-standing and flexible Nb-NC/I_2 composite cathode with a thickness of ~100 μm (Figure S11). The electrochemical performances of Zn-I_2 cells were tested using cathodes made from Nb-NC/I_2, NC/I_2, and Fe-NC/I_2 to compare their effectiveness. One critical issue in Zn-I_2 batteries is the self-discharge phenomenon caused by the repeated shuttling of polyiodides. Therefore, suppressing the shuttle effect during resting time is crucial to enable the good storage performance of batteries. As shown in Figure 4a, the improved voltage maintenance after 100 h for the cell with Nb-NC/I_2 cathode indicates that Nb-NC can effectively adsorb polyiodides, thereby inhibiting the self-discharge behavior of Zn-I_2 batteries. In situ electrochemical impedance spectroscopy (EIS) was conducted during the initial charge-discharge cycle to assess the charge-transfer behavior of different cathodes. The charge-transfer resistance of Nb-NC/I_2 electrode (28.34 Ω) at the

View Article Online
DOI: 10.1039/D4EE04109D

pristine state is notably smaller than that of NC/I_2 electrode (111.46 Ω). Throughout the charging and discharging process, the Nb-NC/I_2 electrode consistently maintains a much smaller interfacial resistance (Figure 4b and S12), demonstrating that the incorporation of Nb alters the electronic state of the carbon framework, improving the electrical conductivity and enhancing the reaction kinetics of iodine species.

The rate performance of both Nb-NC/I_2 and NC/I_2 electrodes was further tested under varying current densities ranging from 0.2 to 20 A g^{-1} (Figure 4c). The Nb-NC/I_2 cathode demonstrates a specific capacity of up to 250 mAh g^{-1} at 0.2 A g^{-1} and remains a high specific capacity of 106 mAh g^{-1} as the current density is increased to 20 A g^{-1}. When the current density returns to 0.2 A g^{-1}, a specific capacity of 216 mAh g^{-1} can be recovered. Such excellent rate performance and reversibility of Nb-NC/I_2 cathode are far superior to those of NC/I_2 and widely adopted Fe-NC/I_2 cathodes (Figure S13). Notably, even at a high cycling rate of 10 A g^{-1}, Nb-NC/I_2 electrode could still deliver a specific capacity of ~140 mAh g^{-1} and stable cycling over 50,000 cycles with only 0.00008% capacity decay per cycle, whereas the NC/I_2 electrode only deliver a specific capacity of ~60 mAh g^{-1} under the same conditions. This excellent cycling stability of Nb-NC/I_2 is superior to many representative I_2 cathodes reported previously (Figure 4d and 4f).[30–38] Furthermore, it is often overlooked but especially crucial to maintain stable long-term cycling at a low cycling rate (0.5-1 C)and high loading conditions for practical applications.[39,40] Therefore, the Zn||Nb-NC/I_2 cell were assembled for long cycling test at 0.2 A g^{-1} (1 C) (Figure S14). Even at such a relatively low cycling rate, the Zn||Nb-NC/I_2 cell could still demonstrate a stable long cycle with a specific capacity of 170 mAh g^{-1}, while the Zn||Fe-NC/I_2 cell exhibits a slightly lower capacity. The Zn||Nb-NC/I_2 pouch cell with a loading mass of ~9 mg cm^{-2} could also perform up to 1500 cycles, maintaining a capacity of 1.12 mAh cm^{-2} at 0.2 A g^{-1} (Figure 4e).

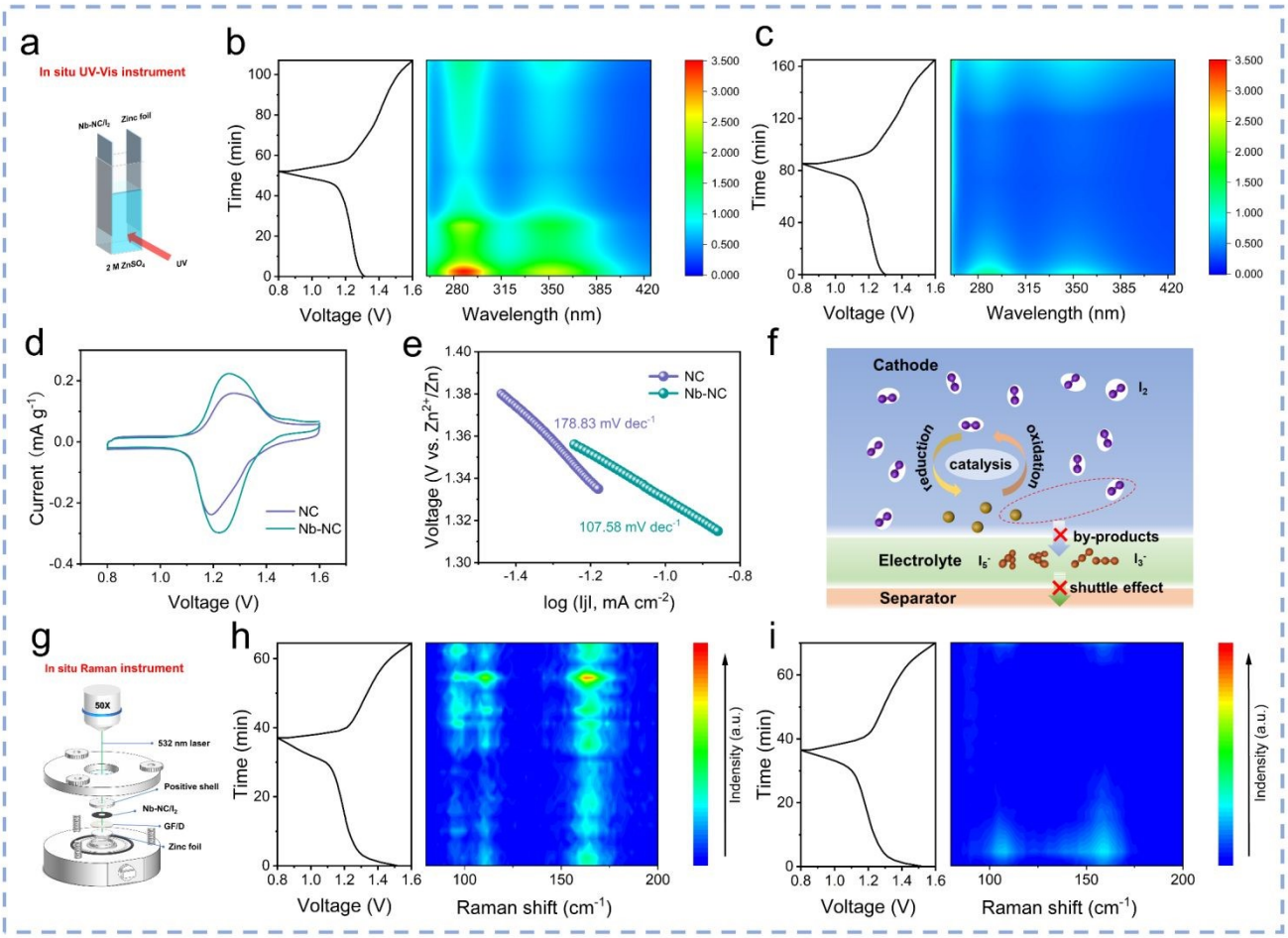

Fig. 5. (a) Schematic diagram of in situ UV-Vis experiment. In situ UV-Vis spectra for (b) NC/I_2 and (c) Nb-NC/I_2 electrodes during the charge-discharge process. (d) The CV curves for Nb-NC/I_2 and NC/I_2 electrodes at 0.1 mV s^{-1}. (e) Tafel curves for Nb-NC/I_2 and NC/I_2 electrodes at 0.2 mV s^{-1}. (f) Schematic illustrations of adsorption and catalysis effect of Nb-NC on polyiodide. (g) Schematic diagram of in situ Raman experiment. In situ Raman spectra for (h) NC/I_2, and (i) Nb-NC/I_2 electrodes

Based on the excellent electrochemical performance of Nb-NC/I_2 electrodes achieved in Zn-I_2 batteries, further ex/in situ characterizations were conducted to get deeper insights into the underlying adsorption and catalysis mechanisms of Nb-NC. As the I_2 electrode generates polyiodide dissolved in the electrolyte during the charging and discharging process, which results in deterioration of electrochemical performance, the adsorption capacities of NC and Nb-NC on polyiodide were first

View Article Online
DOI: 10.1039/D4EE04119D

verified. To assess this, 5 mg of NC powder and 5 mg of Nb-NC powder were each placed in 4 mL of $Zn(I_3)_2$ solution (prepared by mixing I_2 and ZnI_2 in deionized water at a molar ratio of 2:1 with continuous stirring to obtain a 4 mM $Zn(I_3)_2$ solution). The color changes of solutions were observed over time: the solution containing Nb-NC powder shows a lighter color after the same resting time (Figure S15). To make quantitative comparisons, the corresponding standard plots revealing the relationship between concentration and absorbance were obtained by measuring the absorbance of $Zn(I_3)_2$ solution with different concentrations (Figure S16). The concentration of I_3^- in solution containing Nb-NC and NC powder after 24 h was calculated by substituting the absorbance at this point in the standard curve as 0.208, and 0.344 mM respectively, indicating that Nb-NC had a significantly higher absorption capacity compared to NC.

The impact of differences in adsorption capacity on the formation of polyiodide during electrochemical processes was preliminarily investigated by in situ Ultraviolet-visible (UV-vis) spectra using a homemade electrochemical cell (Figure 5a). The characteristic absorption wavelengths of two peaks located at 288 and 350 nm are attributed to I_3^-. During the discharging process, these spectral peaks of I_3^- gradually diminish, attributed to the transition from I_3^- to I^-. Conversely, during the charging process, the peaks associated with I_3^- reappear and intensity as the charging potential increases, reaching their strongest level at 1.6 V. The obvious weaker peak intensity of I_3^- in the electrolyte of Zn||Nb-NC/I_2 cell throughout the process (Figure 5b) compared with that of Zn||NC/I_2 cell (Figure 5c) indicates that there is relatively less polyiodide dissolved in the electrolyte during cycling, proving that Nb-NC possesses a stronger ability to adsorb I_3^- compared to NC. It has demonstrated that the shuttle effect of polyiodide will also result in the corrosion of zinc anode and the generation of by-products. Therefore, the XRD patterns of zinc foils after cycling were conducted to confirm the suppressed shuttle effect (Figure S17). The $Zn_4SO_4(OH)_6{\cdot}5H_2O$ by-product was detected on the zinc foil after 50 cycles in the Zn||NC/I_2 cell, while a weaker by-product signal was observed in the Zn||Nb-NC/I_2 cell. Furthermore, Nb-NC/I_2 cathode is coupled with a thinner Zn anode (30 μm) to prove the feasibility (Figure S18). Even at a small current density of 0.2 A g^{-1}, the Nb-NC/I_2 cathode still maintain stable for more than 500 cycles, further verifying the corrosion of Zn metal anodes can be suppressed through the inhibited polyiodide shuttling in Zn||Nb-NC/I_2 cell.

The catalytic effect of the Nb-NC on the kinetics of the reaction between iodine species during the redox process was investigated by cyclic voltammetry (CV) measurements. The redox peaks in the CV curves are attributed to the conversion of I_2/I^-, and the higher peak currents and lower polarization of Nb-NC/I_2 proves that Nb-NC possesses a better catalytic activity (Figure 5d). It has been demonstrated that low Tafel slope (η) corresponds to fast reaction kinetics and better catalytic activity.[41] As can be obtained from the data in Figure 5e, Nb-NC/I_2 electrode exhibited the lower η of 107.58 mV dec^{-1}, compared with 178.83 mV dec^{-1} for NC/I_2 electrode, indicating the faster reaction kinetics of the Nb-NC/I_2 electrode. To demonstrate the effective restrain of polyiodide generation by Nb-NC host with high adsorption capacity and catalyst activity, in situ Raman measurements were conducted (Figure 5g). The peaks initially located at 110 and 166 cm^{-1} are attributed to I_3^- and I_5^-, which are consistently weak during the whole charging and discharging process in the Zn||Nb-NC/I_2 cell (Figure 5h). In the case of Zn||NC/I_2 cell, the peak intensities of polyiodide remain strong (Figure 5i), indicating weak adsorption of polyiodide by NC and incomplete conversion of polyiodide during cycling. In summary, the free-standing Nb-NC/I_2 electrode can efficiently adsorb polyiodide and enhance iodine redox conversion, thereby ensuring outstanding rate capability and durable cycling stability (Figure 5f).

Conclusions

In summary, DFT calculations are utilized as a preliminary strategy to explore how different d-block SACs in the form of M-N_4 (M= Co, Cu, Fe, Nb, Ni, Zn, Mo, Re, Rh, W, Ru, Ti) configurations affect the polyiodide conversion reaction following the d-p orbital hybridization theory. Among different d-block SACs studied, Nb possesses fewer d-orbital electrons, and a rearrangement of the d-orbital energy levels is verified in Nb-NC. Nb–NC with abundant unfilled antibonding states and a d-band center of 0.271 eV near the Fermi level, enables more effective d–p orbital hybridization, thus providing a strong iodine affinity and rapid iodine redox kinetics. Calculations further reveal that Nb-NC possesses the highest binding energy for polyiodide and the lowest reaction barrier for the rate-determining step ($I_3^- \rightarrow I^-$). Motivated by this theoretical proposal, Nb-NC is synthesized and adopted as an efficient electrocatalyst for Zn-I_2 batteries. Various in/ex situ experimental characterizations demonstrate that the shuttle effect of polyiodide is effectively suppressed and the electrocatalytic redox conversion of iodine is enhanced. Consequently, the Zn||Nb-NC/I_2 battery delivered a long-cycling stability of 50,000 cycles even at a high current density of 10 A g^{-1} (140 mAh g^{-1} with a capacity retention of 96%).

Author contributions

J. Y, and Y. K. contributed equally to this work. Conceptualization: J. Y, Y. K, J. Z and Y. Y. Experimental design and investigation: J. Y and Y. K. Data analyses: J. Y, Y. K, F. M, W. M, G. C, M. Z, Z. L, Z. W, C. L, J. Z, and Y. Y. Calculation: Y. K. Writing-original draft: J. Y. Writing-review & editing: J. Y, C. L, J. Z, and Y. Y.

Conflicts of interest

There are no conflicts to declare.

Data availability

The data that support the findings of this study are available from the corresponding author upon reasonable request.

View Article Online
DOI: 10.1039/D4EE04119D

Acknowledgements

The authors gratefully acknowledge the financial support from National Natural Science Foundation of China (No. 22379125, 22109030, and 22021001), Fundamental Research Funds for the Central Universities (20720220073), Fujian Industrial Technology Development and Application Plan (2022I0002), Key Research and Development Program Project of the Xinjiang Autonomous Region (2023B01025-1). The numerical calculations in this paper have been done on Hefei advanced computing center.

Notes and references

1 Chinese Society of Electrochemistry, *Journal of Electrochemistry*, 2024, 30(1): 2024121. DOI: 10.61558/2993-074X.3444
2 L. Lin, Z. Lin, J. Zhu, K. Wang, W. Wu, T. Qiu and X. Sun, *Energy Environ. Sci.*, 2023, **16**, 89–96.
3 Y. Song, P. Ruan, C. Mao, Y. Chang, L. Wang, L. Dai, P. Zhou, B. Lu, J. Zhou and Z. He, *Nano-Micro Lett.*, 2022, **14**, 218.
4 J. Ke, Z. Wen, Y. Yang, R. Tang, Y. Tang, M. Ye, X. Liu, Y. Zhang and C. Li, *Adv. Funct. Mater.*, 2023, **33**, 2301129.
5 S. Zheng, L. Wei, Z. Zhang, J. Pan, J. He, L. Gao and C. Li, *Nano Lett.*, 2022, **22**, 9062–9070.
6 S. Zhang, J. Hao, H. Wu, Q. Chen, C. Ye and S. Qiao, *Advanced Materials*, 2024, 2404011.
7 T. Liu, C. Lei, H. Wang, J. Li, P. Jiang, X. He and X. Liang, *Advanced Materials*, 2024, 2405473.
8 J. Ma, M. Liu, Y. He and J. Zhang, *Angew Chem Int Ed*, 2021, **60**, 12636–12647.
9 M. Wang, Y. Meng, M. Sajid, Z. Xie, P. Tong, Z. Ma, K. Zhang, D. Shen, R. Luo, L. Song, L. Wu, X. Zheng, X. Li and W. Chen, *Angew Chem Int Ed*, 2024, e202404784.
10 Y. Liu, F. Li, J. Hao, H. Li, S. Zhang, J. Mao, T. Zhou, R. Wang, L. Zhang and C. Zhang, *Adv. Funct. Mater.*, 2024, **34**, 2400517.
11 J. Hao, S. Zhang, H. Wu, L. Yuan, K. Davey and S. Qiao, *Chem. Soc. Rev.*, 2024, **53**, 4312–4332.
12 S. Huang, R. Tang, X. Liu, Y. Zhang, Y. Tang, Z. Wen, M. Ye, Y. Yang and C. C. Li, *Energy Environ. Sci.*, 2024, **17**, 591–601.
13 L. Zhang, H. Guo, W. Zong, Y. Huang, J. Huang, G. He, T. Liu, J. Hofkens and F. Lai, *Energy Environ. Sci.*, 2023, **16**, 4872–4925.
14 L. Ma, G. Zhu, Z. Wang, A. Zhu, K. Wu, B. Peng, J. Xu, D. Wang and Z. Jin, *Nano Lett.*, 2023, **23**, 5272–5280.
15 J. Yang, Z. Yu, J. Wu, J. Li, L. Chen, T. Xiao, T. Xiao, D. Cai, K. Liu, P. Yang and H. J. Fan, *Advanced Materials*, 2023, **35**, 2306531.
16 W. Li, H. Xu, H. Zhang, F. Wei, T. Zhang, Y. Wu, L. Huang, J. Fu, C. Jing, J. Cheng and S. Liu, *Energy Environ. Sci.*, 2023, **16**, 4502–4510.
17 J. L. Yang, H. H. Liu, X. X. Zhao, X. Y. Zhang, K. Y. Zhang, M. Y. Ma, Z. Y. Gu, J. M. Cao and X. L. Wu, *J. Am. Chem. Soc.*, 2024, **146**, 6628–6637.
18 F. Wang, W. Liang, X. Liu, T. Yin, Z. Chen, Z. Yan, F. Li, W. Liu, J. Lu, C. Yang and Q. Yang, *Adv. Energy Mater.*, 2024, **14**, 2400110.
19 W. Liu, P. Liu, Y. Lyu, J. Wen, R. Hao, J. Zheng, K. Liu, Y. Li and S. Wang, *ACS Appl. Mater. Interfaces*, 2022, **14**, 8955–8962.
20 Q. Zhao, Y. Lu, Z. Zhu, Z. Tao and J. Chen, *Nano Lett.*, 2015, **15**, 5982–5987.
21 X. Guo, H. Xu, Y. Tang, Z. Yang, F. Dou, W. Li, Q. Li and H. Pang, *Advanced Materials*, 2024, 2408317.
22 L. Zhang, D. Liu, Z. Muhammad, F. Wan, W. Xie, Y. Wang, L. Song, Z. Niu and J. Chen, *Advanced Materials*, 2019, **31**, 1903955.
23 Y. Zhang, C. Kang, W. Zhao, Y. Song, J. Zhu, H. Huo, Y. Ma, C. Du, P. Zuo, S. Lou and G. Yin, *J. Am. Chem. Soc.*, 2023, **145**, 1728–1739.
24 Z. Han, S. Zhao, J. Xiao, X. Zhong, J. Sheng, W. Lv, Q. Zhang, G. Zhou and H. Cheng, *Advanced Materials*, 2021, **33**, 2105947.
25 W. Qu, J. Zhu, G. Cao, S. Chen, Y. Tan, B. Chen and M. Zhang, *Small*, 2024, **20**, 2310475.
26 X. Yang, H. Fan, F. Hu, S. Chen, K. Yan and L. Ma, *Nano-Micro Lett.*, 2023, **15**, 126.
27 F. Yang, J. Long, J. A. Yuwono, H. Fei, Y. Fan, P. Li, J. Zou, J. Hao, S. Liu, G. Liang, Y. Lyu, X. Zheng, S. Zhao, K. Davey and Z. Guo, *Energy Environ. Sci.*, 2023, **16**, 4630–4640.
28 M. Liu, Q. Chen, X. Cao, D. Tan, J. Ma and J. Zhang, *J. Am. Chem. Soc.*, 2022, **144**, 21683–21691.
29 C. Guo, Y. Cao, Y. Gao, C. Zhi, Y. Wang, Y. Luo, X. Yang and X. Luo, *Adv. Funct. Mater.*, 2024, **34**, 2314189.
30 L. Zhang, J. Ge, T. Wang, H. Guo, S. Chen, Y.-E. Miao, E. Debroye, G. He, I. P. Parkin, J. Hofkens, F. Lai and T. Liu, *Nano Lett.*, 2024, **24**, 3036–3043.
31 X. Yang, H. Fan, F. Hu, S. Chen, K. Yan and L. Ma, *Nano-Micro Lett.*, 2023, **15**, 126.
32 F. Yang, J. Long, J. A. Yuwono, H. Fei, Y. Fan, P. Li, J. Zou, J. Hao, S. Liu, G. Liang, Y. Lyu, X. Zheng, S. Zhao, K. Davey and Z. Guo, *Energy Environ. Sci.*, 2023, **16**, 4630–4640.
33 K. Wang, H. Li, Z. Xu, Y. Liu, M. Ge, H. Wang, H. Zhang, Y. Lu, J. Liu, Y. Zhang, Y. Tang and S. Chen, *Adv. Energy Mater.*, 2024, 2304110.
34 J. Ma, A. Azizi, E. Zhang, H. Zhang, A. Pan and K. Lu, *Chem. Sci.*, 2024, **15**, 4581–4589.
35 M. Liu, Q. Chen, X. Cao, D. Tan, J. Ma and J. Zhang, *J. Am. Chem. Soc.*, 2022, **144**, 21683–21691.
36 Y. Kang, G. Chen, H. Hua, M. Zhang, J. Yang, P. Lin, H. Yang, Z. Lv, Q. Wu, J. Zhao and Y. Yang, *Angewandte Chemie*, 2023, **135**, e202300418.
37 J. He, H. Hong, S. Hu, X. Zhao, G. Qu, L. Zeng and H. Li, *Nano Energy*, 2024, **119**, 109096.
38 S. Chai, J. Yao, Y. Wang, J. Zhu and J. Jiang, *Chemical Engineering Journal*, 2022, **439**, 135676.
39 C. Li, S. Jin, L. A. Archer and L. F. Nazar, *Joule.*, 2022, **6**, 1733–1738.
40 Z. Xing, G. Xu, J. Han, G. Chen, B. Lu, S. Liang and J. Zhou, *Trends. chem.*, 2023, **5**, 380–392.
41 L. Ma, Y. Ying, S. Chen, Z. Huang, X. Li, H. Huang and C. Zhi, *Angewandte Chemie*, 2021, **133**, 3835–3842.

View Article Online
DOI: 10.1039/D4EE04119D

Data Availability Statement

The data that support the findings of this study are available from the corresponding author upon reasonable request.